Journal of Energy Storage 98 (2024) 112875

Contents lists available at ScienceDirect

Journal of Energy Storage

journal homepage: www.elsevier.com/locate/est

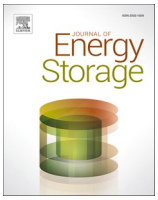

Research papers

Energy storage and melting heat transfer of coconut oil-CuO aluminum open cell composite embedded in a double wavy wall cavity

Ammar I. Alsabery [a,*], Mohammad Ghalambaz [b,c], Ahmad Hajjar [d], Obai Younis [e,f], Ali Akremi [g,h], Mehdi Fteiti [i], Ishak Hashim [j,k]

[a] Refrigeration & Air-conditioning Technical Engineering Department, College of Technical Engineering, The Islamic University, Najaf, Iraq
[b] Department of Mathematics, Saveetha School of Engineering, SIMATS, Chennai, India
[c] Laboratory on Convective Heat and Mass Transfer, Tomsk State University, 634050 Tomsk, Russia
[d] Center for Environmental Intelligence and College of Engineering and Computer Science, VinUniversity, Hanoi, Viet Nam
[e] Department of Mechanical Engineering, College of Engineering in Wadi Alddwasir, Prince Sattam Bin Abdulaziz University, Saudi Arabia
[f] Department of Mechanical Engineering, Faculty of Engineering, University of Khartoum, Sudan
[g] Department of Chemistry, Faculty of Science, Northern Border University, Arar, Saudi Arabia
[h] Department of Chemistry, High Institute of Environmental Sciences and Technologies, Carthage University, Borj Cedria, Tunisia
[i] Physics Department, Faculty of Science, Umm Al-Qura University, Makkah 24381, Saudi Arabia
[j] Department of Mathematical Sciences, Faculty of Science & Technology, Universiti Kebangsaan Malaysia, 43600 UKM Bangi, Selangor, Malaysia
[k] Nonlinear Dynamics Research Center (NDRC), Ajman University, Ajman PO Box 346, United Arab Emirates

ARTICLE INFO

Keywords:
Energy storage
Melting heat transfer
Taguchi optimization method
Double wavy wall cavity
NePCM

ABSTRACT

The melting heat transfer and thermal energy storage were addressed in a latent heat thermal energy storage (LHTES) unit. The LHTES unit is made of wavy channels filled with Coconut oil-CuO nano-enhanced phase change material (NePCM). The aim is to address the impact of nanoparticles and enclosure wall corrugation of energy storage. The phase change from solid to liquid was based on the enthalpy-porosity method. A mesh adaptation technique was employed to refine the mesh at the melting interface and increase the accuracy and stability of the simulations. The wavy surface design allows more heat transfer surface between the NePCM inside the enclosure and the working fluid. The Taguchi optimization method maximized the melting (thermal charging). The impact of porosity, volume fraction of nanoparticles, and wave number on the melting rate and stored energy were investigated. The results showed that increasing the porosity reduces the melting rate, particularly in the lower regions of the enclosure. Varying the wave number could change the flow and heat transfer patterns, but it showed a minimal impact on the melting rate. The melting rate was maximum for the maximum volume fraction of nanoparticles (nanoparticles volume fraction = 0.05), minimum porosity (0.05), and two undulations (wave number = 2).

Nomenclature

Latin symbols	
A_{mush}	constant with a large number (Pa.s.m^{-2})
C_p	heat capacity (J.kg^{-1}.K^{-1})
dA	differential surface element (m^2)
dl	pore characteristics
d_p	pore density (PPI)
g	gravitational constant (m.s^{-2})
h_f	phase change latent heat (J.kg^{-1})
K	metal foam's permeability (m^2)
MVF	normalized melt volume fraction
n	normal to a surface (m)
N	wave number
p	pressure (Pa)
Pr	Prandtl number
t	time (s)
T	temperature (K)
T_c	cold wall temperature (K)
T_h	hot wall temperature (K)
T_{in}	initial temperature (K)
T_m	fusion temperature (K)
u	x-velocity component (m.s^{-1})

(continued on next column)

(continued)

(continued on next page)

* Corresponding author.
E-mail addresses: ammar_e_2011@yahoo.com (A.I. Alsabery), m.ghalambaz@gmail.com (M. Ghalambaz), ali.akrmi@nbu.edu.sa (A. Akremi).

https://doi.org/10.1016/j.est.2024.112875
Received 6 March 2024; Received in revised form 26 June 2024; Accepted 7 July 2024
Available online 1 August 2024

(*continued*)

v	y-velocity component ($m.s^{-1}$)
$\vec{V}$	velocity vector ($m.s^{-1}$)
x	x-coordinate (m)
y	y-coordinate (m)
Greek symbols	
ES	stored energy (J)
S/N	signal to noise ratio
β	coefficient of the volume expansion (K^{-1})
δ	phase change function
ΔT	phase change temperature interval (K)
$\Delta\lambda$	thermal conductivity difference in Eq. (13) ($W.m^{-1}.K^{-1}$)
ε	metal foam's porosity
λ	thermal conductivity ($W.m^{-1}.K^{-1}$)
μ	dynamic viscosity ($kg.m^{-1}.s^{-1}$)
ρ	density ($kg.m^{-3}$)
χ	parameter of Eq. (13)
ω	nanoparticles fraction
ς	a small constant value
Subscripts	
fu	fusion
l	liquid/molten PCM
na	nanoparticle
NeP	Nano-PCM
PCM	host PCM
pm	porous material – metal foam
pm, eff	effective nano-PCM and metal foam
s	solid PCM

1. Introduction

Thermal energy storage is a promising approach to develop renewable energy [1,2] and waste heat recovery [3,4] technologies. Phase change materials (PCM) absorb/produce notable amounts of latent heat energy in a compact space without a chemical reaction or significant thermal energy loss. Thus, they can fill the discrepancy between supply and demand [5]. Thus, PCMs have been used in buildings [6], power generation systems [7], automotive [8], and solar domestic water heating systems [9].

Even though PCMs are able to store a notable quantity of heat energy in form of latent heat, they suffer from mediocre heat transfer properties due to low thermal conductivity [10]. Therefore, charging and discharging latent heat thermal energy storage (LHTES) units is slow and takes a long time. This is while a quick store/release of energy in many applications is critically required. As a result, many researchers focused on enhancing the thermal conductivity and heat transfer properties of LHTES units by using nano-additives [11,12], fins [13,14], metallic foams [15], and encapsulation techniques [15,16].

Using wavy surfaces is an interesting approach to raise the heat transfer area and improve the rate of thermal energy storage. The wavy surface approach was investigated by Revnic et al. [17]; they explored the impact of using a wavy surface wall and hybrid nanofluids on the heat transfer enhancement of hybrid nanofluids. The authors described the mechanisms of the natural convection and conduction heat transfer in the wavy enclosure. Saleem et al. [18] examined the free convection of rarefied gaseous flows in a square enclosure with wavy walls. They discussed the heat transfer mechanism in the cavity and noted that its shape characteristics have a considerable impact on the heat transfer rate. Ganesh et al. [19] considered the free convection heat transfer in an enclosure with wavy upper and bottom walls. The enclosure contained a non-Newtonian fluid. The authors discussed the impact of waviness on the thermal performance of enclosure in the presence of non-Newtonian effects. The outcomes revealed that the amplitude of waviness could enhance the heat transfer rate by 116 %.

Some authors utilized porous material in the wavy enclosures to control the natural convection flow field and heat transfer. For example, Biswas et al. [20] investigated the free convection heat transfer of hybrid nanofluids in a double-wavy wall enclosure. Compared to a plain vertical wall, their findings show that the wavy walls could promote heat transfer by about 22 %. They also noticed that the strength of circulation could be reduced in the enclosure. In a subsequent work, Biswas et al. [21] studied the effect of wall undulation (waviness) on the free convection heat transfer in a wavy wall chamber. They found that the waviness could be optimal for four undulations and a normal amplitude of 0.3. Moreover, in the book of Shenoy et al. [22], various aspects of heat transfer and thermal convection from undulated surfaces, such as porous media, viscous fluids, and nanofluids, were examined. The integration of PCMs with metal foams has shown promise in enhancing the thermal performance of energy storage systems. Recent studies have focused on optimizing the configuration and positioning of metal foams to minimize energy storage losses while maximizing melting performance. A comprehensive numerical analysis revealed that various metal foam shapes, including kite, triangular, and square, can significantly reduce melting times by up to 74.8 % compared to non-porous designs, with kite-shaped foam proving to be the most economically effective [23]. Further investigations have demonstrated that incorporating nanoparticles into PCMs can increase the melting rate by about 8 % but at the cost of a slight reduction in stored energy [24].

Some recent studies also considered the case of nano-enhanced phase change material suspensions in wavy wall enclosures. In these studies, the phase change nanoparticles are added to a liquid to synthesize a nanofluid with phase change nanoparticles. In such investigations, it must be noted that the core of nanoparticles undergoes a phase change, and there is no solid/liquid interface or solid region in the enclosure. Therefore, the heat transfer mechanisms in such studies can be viewed and analyzed using the natural convection studies approaches discussed above. For example, Aly et al. [25–27] addressed the convective flow of nano-enhanced phase change material suspensions in enclosures with curved walls. These studies aim to use the latent heat of nanoparticles to improve the heat transfer characteristics of a working fluid. Typically, the energy storage aspects of the liquid are not of concern.

The literature review shows that the wavy surfaces have been extensively explored in the context of free convection in enclosures. However, only a few studies assessed the effect of utilizing wavy enclosures on the phase change heat transfer of PCM in LHTES units. Singh and Negi [28] utilized a wavy fin design to improve heat transfer in a solar collector integrating a PCM layer for thermal storage. The wavy fins were in contact with a cold flow, but they were in contact with the PCM through a flat plate above the PCM layer. They found that wavy fins on the top of a PCM layer could efficiently provide high thermal efficiency and energy storage in all solar situations. In an interesting study, Ma et al. [29] used a wavy channel LHTES to cool the air in buildings. The air passage was a wavy channel that was in contact with a PCM chamber. In their model, the wavy walls were located at the bottom/top of the PCM chamber. The founding revealed that using a wavy wall air passage could improve heat transfer and accelerate solidification. Iachachene et al. [30] investigated natural convection melting of phase change materials in corrugated porous cavities, highlighting the effects of porosity and wall undulations. Lower porosity (80–96 %) enhances melting rates, while strategic heater placement and increased undulations can reduce melting time by 27.4 % and increase energy storage by 11.36 %. Studies show that semicircular enclosures can improve thermal response by reducing unmelted volume and accelerating melt dynamics [31]. Additionally, integrating wavy PCM units with porous media in solar air heaters has optimized power and energy density, achieving significant temperature gains and prolonged thermal energy storage [32]. Shahsavar et al. [33] performed an investigation on the phase change heat transfer and thermal energy storage in the space between two tubes of a shell-and-tube shape exchanged. The inner tube was a wavy tube, and the outer tube was flat. The PCM layer was enclosed between the inner and outer tubes. The waviness of the tube was varied along the tube length. Compared with a straight tube, the results showed that the melting (solidification) time case declined 70.8 % (42.8 %), respectively.

The literature review indicates that wavy surfaces enhance free convection in enclosures and increase surface heat transfer in LHTES

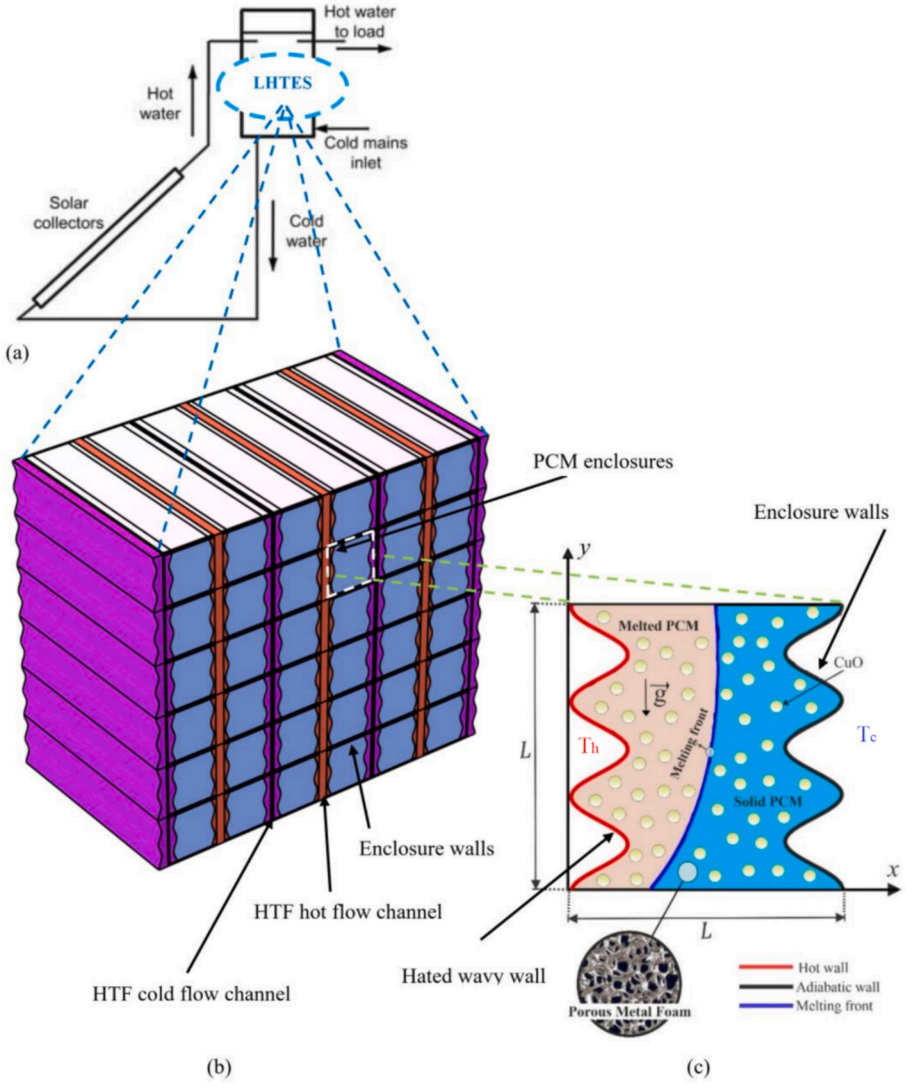

Fig. 1. Schematic physical description of the used NePCM-porous wavy cavity: (a) A simple solar thermal LHTES; (b) A latent heat thermal energy storage with hot and cold channels; (c) A model of wavy wall latent heat thermal energy storage enclosure.

Table 1
Thermophysical Characteristics of nanoparticles, metal foam, PCM, and nano-PCM.

Property (units)	Coconut oil (measured) [36]			CuO nanoparticle [37]	Aluminum [38]
State	Solid ($15^{\circ}C$)	Liquid ($32^{\circ}C$) (ω_{na} = 0%)	Liquid ($32^{\circ}C$) (ω_{na} = 0.1%)		
μ (N s/m^2)	–	$0.0326 \pm 3\%$	$0.0332 \pm 3\%$	–	–
ρ (kg/m^3)	920	$914 \pm 0.11\%$	$916 \pm 0.11\%$	2700	6500.0
C_p (J/kg K)	3750	$2010 \pm 0.2\%$	$2001 \pm 0.2\%$	897	540
h_f (kJ/kg)	–	$103 \pm 1\%$	$101 \pm 1\%$	–	–
k (W/m K)	0.228	$0.166 \pm 1.2\%$	$0.174 \pm 3.7\%$	205	18.0
Pr	–	$394.73 \pm 3.2\%$	$381.80 \pm 4.8\%$	–	–
T_{fu}	$24^{\circ}C$ ($\pm 1^{\circ}C$)	–	–	–	–

units. However, it also indicates that surface waviness can affect convection flow mechanisms and heat transfer within cavities. Notably, the integration of nanoparticles, metal foams, and wavy surfaces for heat transfer enhancement has not been thoroughly explored in existing studies. This study is the first to investigate the thermal behavior and energy storage capabilities of an LHTES unit with a wavy wall, filled with metal foam and nanoparticles.

2. Mathematical model

A LHTES unit is made of wavy shape channels filled with PCM-aluminum foam composites. The hot working fluid flows along the channel walls, maintaining them at a high temperature T_h. The working fluid and PCMs are on opposite sides of the channel walls, transferring heat through the thin walls. Similarly, the cold water for discharging porpoise is following in another channel as depicted in Fig. 1. It is assumed

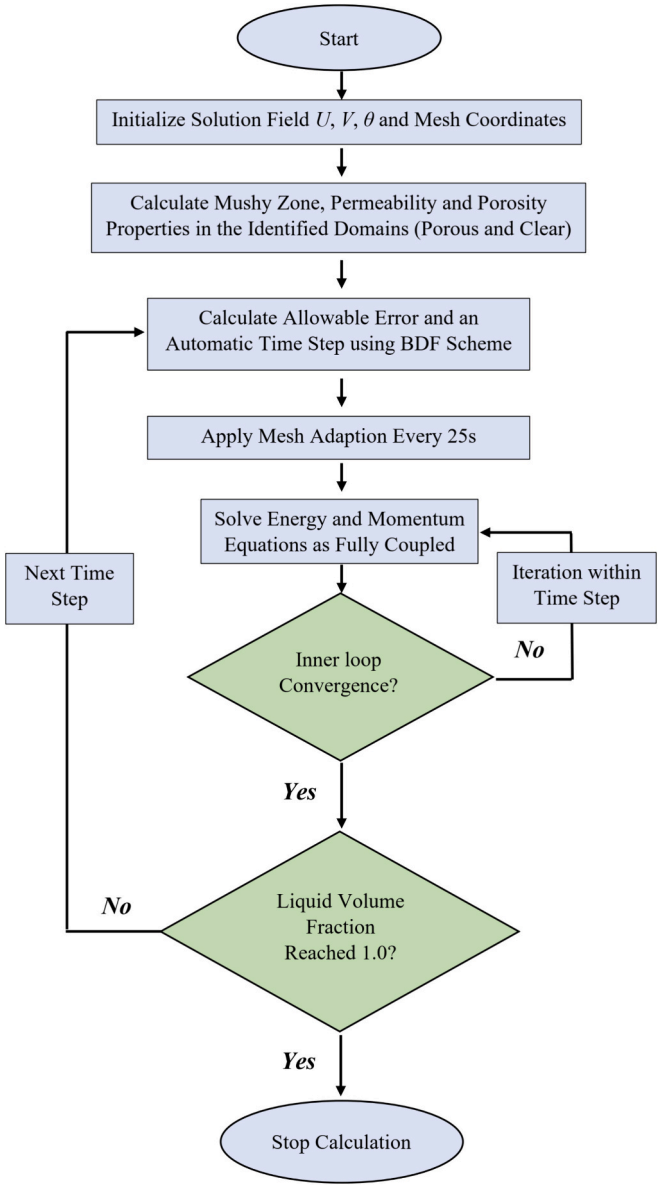

Fig. 2. Flow diagram of the numerical method and solution steps.

that the water flow rate is high, and thus, the enclosure walls the same as the working fluid temperature. A schematic view of the LHTES unit and the PCM-aluminum channel is depicted in Fig. 1. The left wavy wall is at hot temperature T_h while the right wavy wall is at low temperature T_c. The PCM is Coconut oil which is embedded in an open cell aluminum foam, where their thermophysical properties are listed in Table 1. The data have been provided with their measurement errors. However, here the measurement errors were neglected and the main measured values were adopted for the computations.

Coconut oil was adopted in the present study due to its environmentally friendly and organic nature. This PCM has a low fusion temperature, making it a good candidate for low-temperature energy recovery in cold climates. Spherical CuO nanoparticles were chosen because they are stable and do not increase the viscosity of the liquid PCM. Coconut oil is a viscous PCM, and any further increase in viscosity would decrease the natural convection effects and reduce the overall charging/discharging rate. Other nanoparticle choices, such as carbon nanotubes, lead to a notable increase in liquid PCM viscosity and non-Newtonian effects due to the particles' long length [34,35]. Therefore, CuO nanoparticles have been adopted.

It was assumed that the nano-PCM is a uniform mixture of nanoparticles and PCM, and remains uniform during the thermal energy storage and release cycles. Natural convection flow occurs in the liquid PCM due to buoyancy forces, and this flow remains laminar. The Boussinesq approximation was used to model the buoyancy forces. In this model, the thermophysical properties are constant except for the body forces, which drive fluid flow due to buoyancy effects. The overall volume of the nano-PCM remains constant; thus, the impact of total density changes was neglected. The nanoparticles are tiny and therefore are in thermal equilibrium with the host PCM.

2.1. Governing equations and boundary conditions

The control equations of the governing physics are the conservation of mass, momentum and energy as the following [39–41]:

Mass conservation equation:

$$\nabla\cdot\vec{V}=0 \tag{1}$$

$$\frac{\rho_{NeP,l}}{\varepsilon^2}\left[\varepsilon^{-1}\frac{\partial u}{\partial t}+\left(\vec{V}\cdot\nabla\right)u\right]+\frac{\partial p}{\partial x}-\frac{\mu_{NeP,l}}{\varepsilon}\nabla^2u+\frac{\mu_{NeP,l}}{K}u+A_{mush}\frac{(1-\delta(T))^2}{\delta^3(T)+\varsigma}u=0 \tag{2}$$

Momentum conservation equations:

$$\frac{\rho_{NeP,l}}{\varepsilon^2}\left[\varepsilon^{-1}\frac{\partial u}{\partial t}+\left(\vec{V}\cdot\nabla\right)v\right]+\frac{\partial p}{\partial y}-\frac{\mu_{NeP,l}}{\varepsilon}\nabla^2v+\frac{\mu_{NeP,l}}{K}v+A_{mush}\frac{(1-\delta(T))^2}{\delta^3(T)+\varsigma}v-\rho_{NeP,l}g\beta_{NeP,l}(T-T_{fu})=0 \tag{3}$$

The subscripts *NeP* and *l* indicate the nano-enhanced PCM and liquid, respectively. Moreover, T_{fu} is the melting temperature, and δ is the volume fraction of molten PCM, introduced as:

$$\delta(T)=\begin{cases}0 & T<T_{fu}-\Delta T/2\\ \dfrac{T-T_{fu}}{\Delta T}+\dfrac{1}{2} & T_{fu}-\Delta T/2<T<T_{fu}+\Delta T/2\\ 1 & T>T_{fu}+\Delta T/2\end{cases} \tag{4}$$

In which the above metal foam's porosity and permeability are noted by ε and K. The permeability of the metal foam, i.e., K, is [42]:

$$K=d_p^2\frac{73\times10^{-5}}{(1-\varepsilon)^{0.224}}\left(d_ld_p^{-1}\right)^{-1.11} \tag{5a}$$

$$\left(d_ld_p^{-1}\right)=1.18\left(\frac{1-\varepsilon}{3\pi}\right)^{0.5}[1-exp(-(1-\varepsilon)/0.04)]^{-1} \tag{5b}$$

in which,

$$d_p=254\times10^{-4}\omega^{-1}\ (PPI) \tag{5c}$$

Energy conservation equation:

$$(\rho C_p)_{pm,eff}\frac{\partial T}{\partial t}+(\rho C_p)_{NeP,l}\left(\vec{V}\cdot\nabla\right)T=\nabla\cdot(\lambda_{pm,eff}\nabla T)-\rho_{NeP,l}h_{f,NeP}\varepsilon\frac{\partial\delta(T)}{\partial t} \tag{6}$$

in which,

$$(\rho C_p)_{pm,eff}=\delta(T)(\rho C_p)_{pm,eff,l}+(1-\delta(T))(\rho C_p)_{pm,eff,s} \tag{7a}$$

$$(\rho C_p)_{pm,eff}=(1-\varepsilon)(\rho C_p)_{pm}+\varepsilon(\rho C_p)_{NeP} \tag{7b}$$

Subscripts *pm*, *eff* denote the metal foam and effective properties, respectively. The solid phase was also indicated by *s*. The effective porous and NePCM's thermal conductivity are:

$$\lambda_{pm,eff}=\delta(T)\lambda_{pm,eff,l}+(1-\delta(T))\lambda_{pm,eff,s} \tag{8a}$$

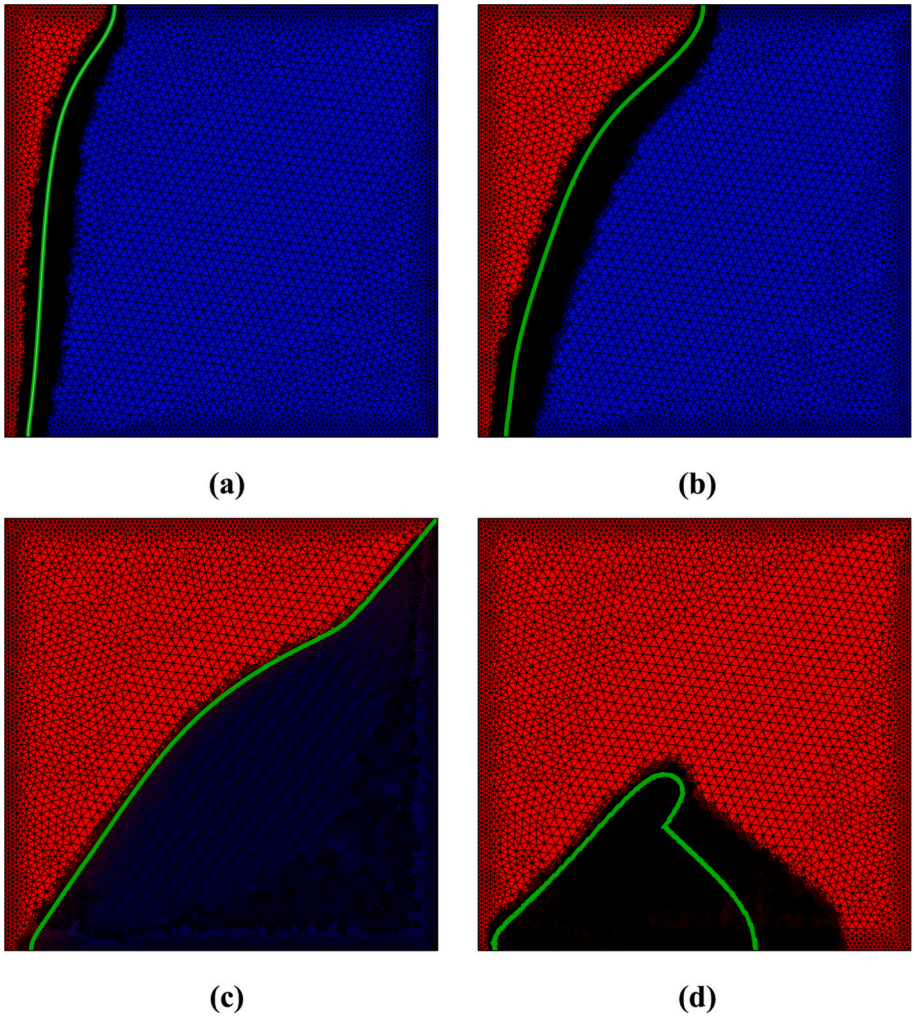

Fig. 3. Adopted for the calculations of the present work for Case III at (a) $t = 1000s$, (b) $t = 2000s$, (b) $t = 4000s$ and (d) $t = 6000s$; the red color is the liquid zone, blue is the solid zone, and the continuous green line represents the melting front for Cu nano-particles for $\varepsilon = 0.9$, $\omega_{na} = 0.04$.(*For interpretation of the references to colour in this figure legend, the reader is referred to the web version of this article.*)

Table 2
Grid testing details for *Cu* nano-particles for $\varepsilon = 0.9$, $\omega_{na} = 0.05$ and $N = 0$.

Cases	Number of domain/boundary elements
Case I	2346/414
Case II	5098/435
Case III	**8005/459**
Case IV	16,704/495
Case V	32,848/607

The porous metallic foam thermal conductivity was calculated as [43,44]:

$$\lambda_{pm,eff} = \frac{\left[\lambda_{NeP} + \pi\left(\sqrt{\chi} - \chi\right)\Delta\lambda\right]\left[\lambda_{NeP} + (\chi\pi)\Delta\lambda\right]}{\lambda_{NeP,i} + \left[\frac{4}{3}\sqrt{\chi}\,(1-\varepsilon) + \pi\sqrt{\chi} - (1-\varepsilon)\right]\Delta\lambda} \tag{9a}$$

in which,

$$\chi = \frac{1-\varepsilon}{3\pi}, \Delta\lambda = \lambda_{pm} - \lambda_{NeP} \tag{9b}$$

The constant temperature of $T_h = 36$ °C and $T_c = 16$ °C was considered for the boundary conditions while the top and bottom walls were well insulated with zero flux. A zero velocity and no slip were applied for the momentum eqs. A zero velocity and $T = T_c$ was assumed for the initial field.

2.2. The thermo-physical properties of the NePCM

The NePCM is considered as a uniform mixture of the PCM and nanoparticles. Thus, its density is evaluated as [45]:

$$\rho_{NeP} = \rho_{PCM} + \omega_{na}(\rho_{na} - \rho_{PCM}) \tag{10a}$$

$$\rho_{PCM}(T) = \rho_{PCM,l}\delta(T) + (1 - \delta(T))\rho_{PCM,s} \tag{10b}$$

in which ω_{na} indicates the nano-additives concentration. The liquid NePCM's dynamic viscosity is computed using the Brinkman model for a uniform mixture as [45,46]:

$$\mu_{NeP,l} = \mu_{PCM,l}(1 - \omega_{na})^{-2.5} \tag{11}$$

where PCM in subscript represents the phase change material with no nanoparticles. The Maxwell model was also utilized to estimate the thermal conductivity of the mixture [47]:

$$\frac{\lambda_{NeP}}{\lambda_{PCM}} = \frac{(\lambda_{na} + 2\lambda_{PCM}) - 2\omega_{na}(\lambda_{PCM} - \lambda_{na})}{(\lambda_{na} + 2\lambda_{PCM}) + \omega_{na}(\lambda_{PCM} - \lambda_{na})} \tag{12}$$

Besides, the NePCM effective heat capacity is computed as the

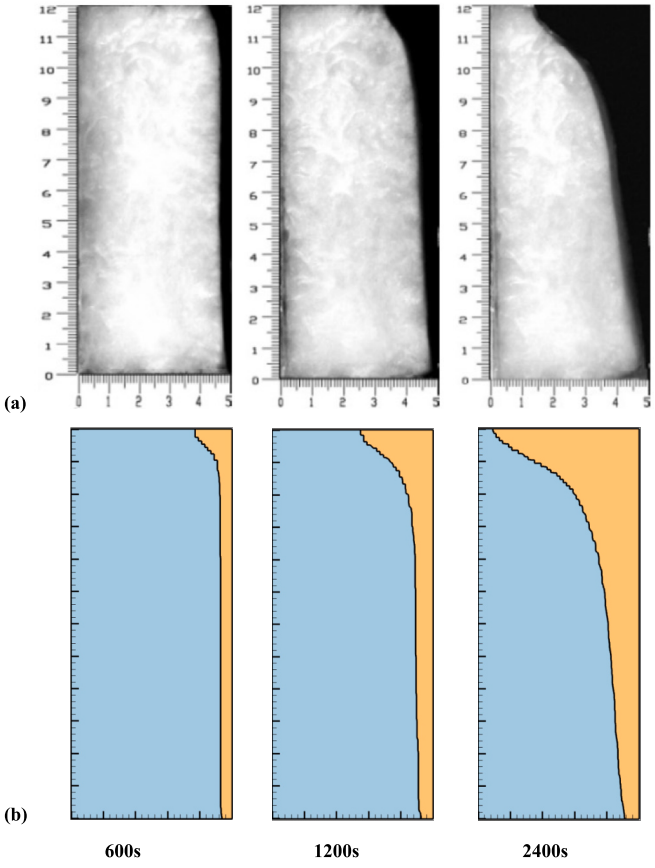

Fig. 4. The melting interface at three time instances (a) reported by [50] and (b) simulated in the present study.

average weight of nanoparticles and PCM as:

$$\rho_{NeP}C_{p,NeP} = \rho_{PCM}C_{p,PCM} + \omega_{na}\left(\rho_{na}C_{p,na} - \rho_{PCM}C_{p,PCM}\right) \tag{13a}$$

$$\rho_{PCM}C_{p,PCM}(T) = \rho_{PCM,l}C_{p,PCM,l}\chi(T) + (1-\chi(T))\rho_{PCM,s}C_{p,PCM,s} \tag{13b}$$

Finally, the effective latent heat of the NePCM is computed as:

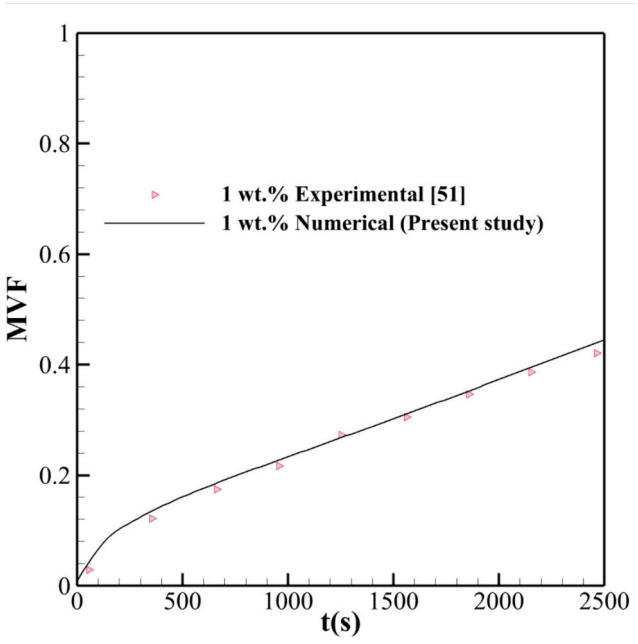

Fig. 6. The melting front computed by the present investigation and those of experimental and numerical reported in [51].

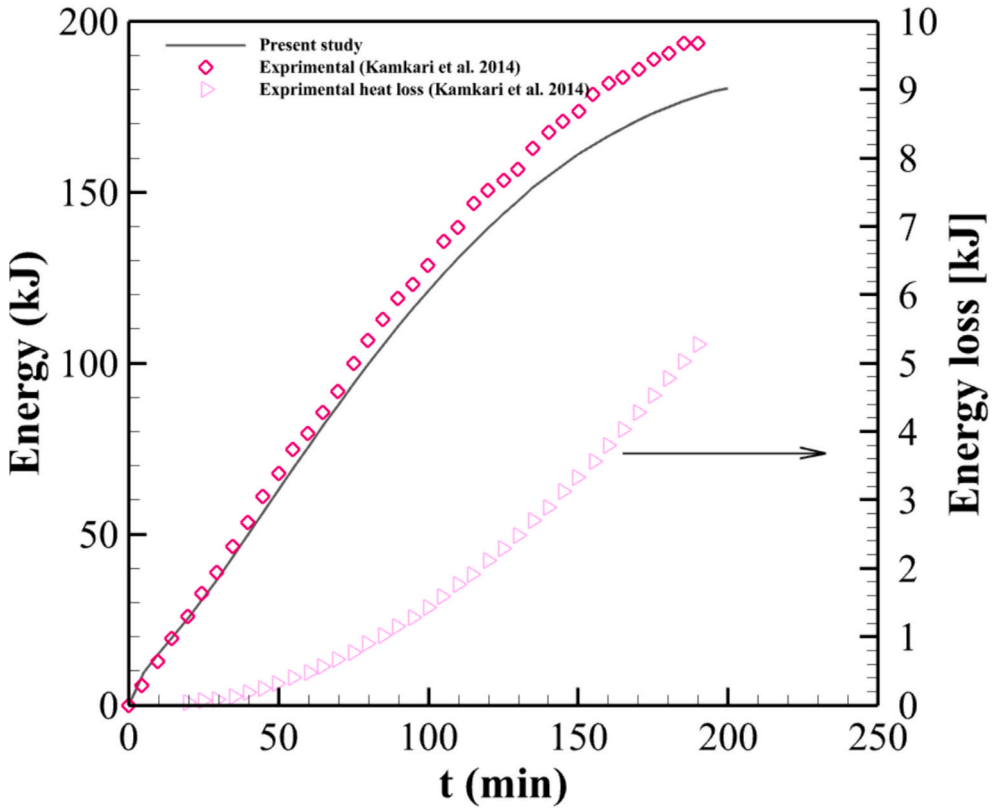

Fig. 5. The stored energy in and melting volume fraction during the melting process reported in [50] and the outcomes of the current research.

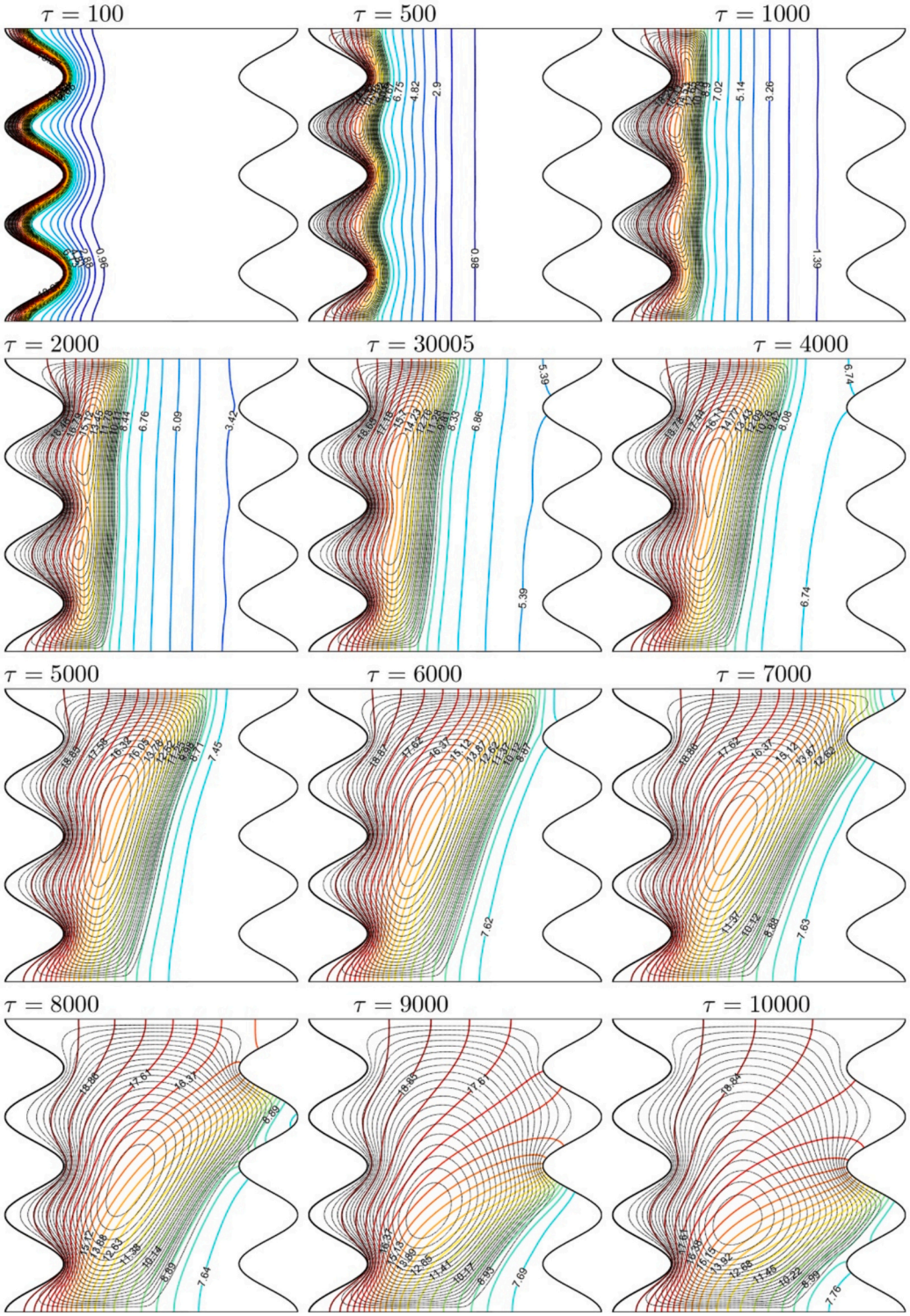

Fig. 7. Isotherms (colored solid lines) and streamlines (dashed lines) evolution at different times for $\omega_{na} = 0.05$, $\varepsilon = 0.9$, $N = 3$.

$$\rho_{NeP,l} h_{f,NeP} = (1-\omega_{na})\rho_{PCM,l} h_{f,PCM} \tag{14}$$

The applied hydrodynamic boundary conditions at all walls are zero velocity. The top, bottom, and right walls are also insulated with zero heat flux. The left wavy wall is at a constant temperature T_h. Thus, the boundary conditions can be represented in a mathematical form as follows

$$\text{The left wavy wall} : u = v = 0, T = T_h \tag{15b}$$

$$\text{The other walls} : u = v = 0, \frac{\partial T}{\partial n} = 0 \tag{15c}$$

where n, the normal direction to the surface, is x or y.

The overall amount of the stored energy is a combination of the latent and sensible heat which can be integrated over all of the domain as:

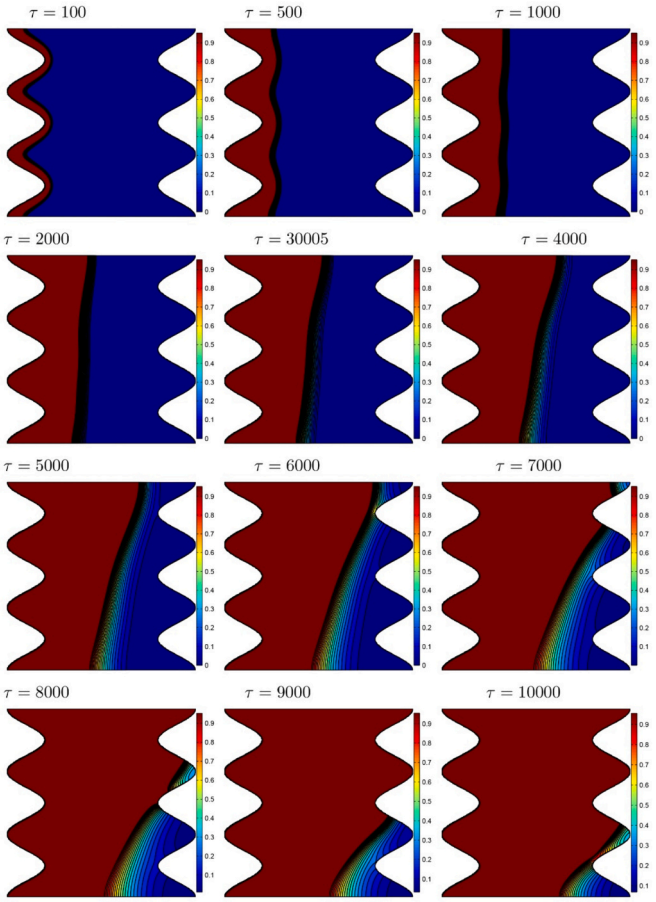

Fig. 8. Melting process evolution at different times for $\omega_{na} = 0.05$, $\varepsilon = 0.9$, $N = 3$.

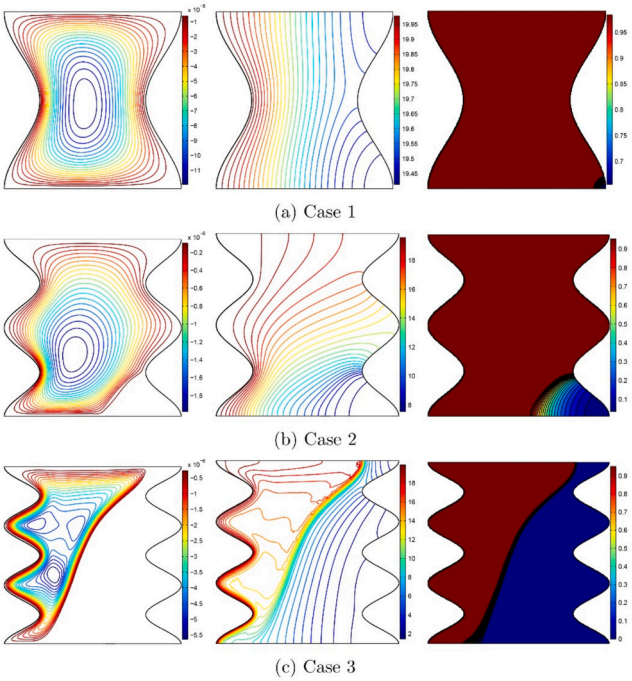

Fig. 9. Streamlines (left), isotherms (middle) and melting process (right) evolution in different cases; $\omega_{na} = 0.0$, $\varepsilon = 0.8$, $N = 1$ (a), $\omega_{na} = 0.025$, $\varepsilon = 0.9$, $N = 2$ (b) and $\omega_{na} = 0.05$, $\varepsilon = 1$, $N = 3$ (c).

$$ES = \int_A \int_{T_{in}}^{T} (\rho C_p)_{eff} dT\, dA + \int_A \rho_{NeP,l} h_{f,NeP} \varepsilon \delta(T) dA \tag{16}$$

In the end, the melting volume fraction is calculated:

$$MVF = \frac{\int_A \varepsilon \delta(T) dA}{\int_A \varepsilon dA} \tag{17}$$

3. Numerical method, grid dependency, and validation

The finite element method was used to solve the governing equations. Additionally, a mesh analysis was conducted to verify the accuracy of the computations. The results were also validated by comparing them with findings from existing literature, ensuring the reliability of the model and outcomes. Further details are included below.

3.1. Numerical method

The governing equations with their boundary conditions were integrated based on the finite element method in a weak form over a descript mesh. The integration results in a set of residual equations solved for the field variables. The flow and heat transfer equations were solved based on Newton's method, where the relative accuracy was set to 10^{-4} [48,49]. An automatic time-step scheme was also employed to actively monitor and control the accuracy below the 10^{-4}. The second order backward differentiation approach was employed for time-step control. The mesh adaptations were checked and employed every 25 s to provide a very fine mesh at the melting interface, mushy region. A diagram of the employed code can be seen in Fig. 2.

3.2. Mesh study

The chosen parameters to test the impact of the grid size on the outcomes are $\varepsilon = 0.9$, $\omega_{na} = 0.05$, and a wave number $N = 0$. The mesh is fine near the walls where there is a high velocity and temperature gradients. Moreover, the mesh adaptation at the melting interface results in a fine mesh which captures the phase, velocity and temperature gradients. As mentioned before, the time-step was controlled automatically using the backward differentiation approach. Thus, here, only the mesh resolution was investigated to ensure the solution accuracy. A view of the melting interface and mesh adaptation is depicted in Fig. 3. Table 2 also shows the number of mesh elements. The details of each mesh study are summarized in Table 2. The analysis of the results showed mesh Case III can provide accurate results. A view of the mesh for case III is plotted in Fig. 3.

3.3. Validation

The results of the current research are compared to the experimental data reported by Kamkari et al. [50] about the melting of paraffin wax in a cavity of size 120 mm (height) and 50 mm (width). The left vertical wall was at a hot temperature of 70 °C. Fig. 4 illustrates the actual images of the melting interface captured by [50] and simulated in the present research. This figure also shows a very good agreement between the experiment and the simulation outcomes. Fig. 5 also, compares the melting fraction and stored energy with the experimental data of [50]. As time progresses, the disparity between the computed energy in this study and the experimental values increases, becoming quite noticeable. This difference, where the computed energy is lower than the experimental results, can likely be attributed to energy losses through the enclosure walls during the experiment. The experiment documented these estimated energy losses, which are illustrated in Fig. 5. These losses closely correspond to the discrepancy between the energy values obtained in the current simulations and those measured experimentally.

Fig. 6 presents a comparison between the measured and simulated melting behaviors of graphene nanoplatelets-tetradecanol (nano-PCM)

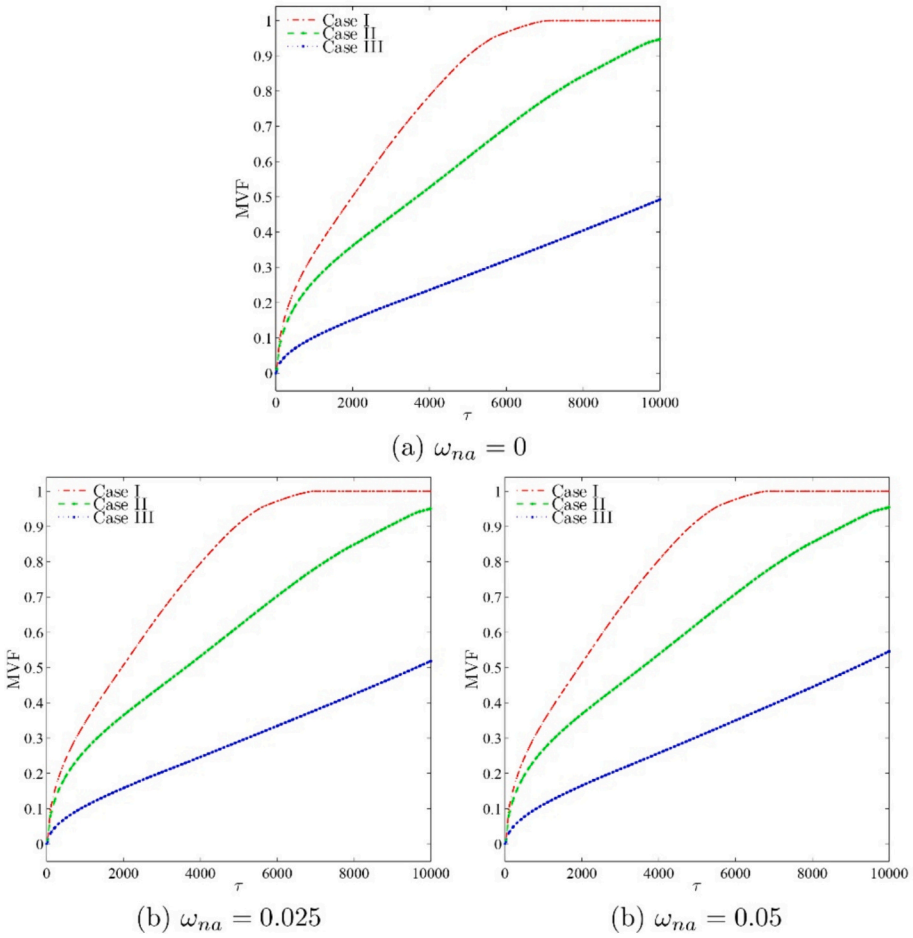

Fig. 10. Melt fraction MVF evolution by different cases and different NeP fractions for $\varepsilon = 0.9$, $N = 3$.

as reported by Li et al. [51]. The experiment took place in a differentially heated enclosure with a height-to-width aspect ratio of 0.8. The enclosure was heated from the left vertical wall and cooled from the right vertical wall, while the top and bottom walls were insulated. The discrepancies between the measured and simulated interfaces are minimal, indicating a reasonable correlation between the experimental and simulation data.

4. Results and discussion

The melting heat transfer is investigated for three cases with different values of Case I: $\omega_{na} = 0.0$, $\varepsilon = 0.8$, $N = 1$, case II: $\omega_{na} = 0.025$, $\varepsilon = 0.9$, $N = 2$, and case III: $\omega_{na} = 0.05$, $\varepsilon = 1$, $N = 3$.

The development of the streamlines and the isothermal contours with time in the cavity is illustrated in Fig. 7. The presence of streamlines indicates that the PCM is in the liquid phase. Initially, the PCM is heated and starts melting near the left wavy wall. As time goes by, more PCM melts, and convective flow starts taking place. The hot liquid moves upwards and is replaced by a colder one, resulting in a clockwise recirculation zone. Due to natural convection, the hot liquid is moving extending the melting region near the top of the cavity compared to its bottom, as evidenced by the larger flow circulation in that region. Upon reaching towards the steady state, most of the enclosure is filled with melted PCM. The presence of a flow separation zone in the wavy walls crests is noted, as the PCM in that zone is detached from the outer flow circulation. The isothermal contours show the transition into the convective flow. In the beginning, the isotherms are ~~vertical,~~ close to each other and parallel to the wavy wall, indicating mainly a conduction-dominated heat transfer. As the convective effects intensify, the isotherms tend to rotate towards the horizontal direction. Near the left wall, the isotherms mimic the wall profile, especially in the bottom zone, illustrating an intensification of heat conduction there. On the other hand, towards the steady state, the coldest zone in the cavity is near the bottom right corner, where PCM melting is delayed compared to the other zones. In that region, the convective effects are weak compared to the top region, where the heat transfer is transferred from the hot liquid towards the cold solid through the melting front. These findings are further validated in Fig. 8 which depicts the melting evolution with time by means of the movement of the melting interface. It is noticed that in the first stages, this interface initially follows the wall profile and then becomes vertical. As time goes on, melting is enhanced in the upper region after convection takes over in the upper region, and the melting interface tilts as more melting takes place upwards. This behavior continues until most of the cavity is covered by liquid PCM, except for the small region near the bottom right corner.

Fig. 9 shows the flow and thermal patterns in the enclosure for three cases, in which different values of the nanoparticle concentration ω_{na}, the porosity ε, and the number of undulations N are varied. It can be seen that the slowest PCM melting is present in case 3, in which all the parameters ω_{na}, ε, and N are at their maximum values. On the other hand, PCM melting is the fastest when these values are minimized. The variation of the melted volume fraction MVF as a function of time is plotted in Fig. 10 for the three cases and for various values of ω_{na}. It is confirmed that case 1 Case I provides the fastest melting, as the value MVF = 1 is reached there first. It is also observed that varying ω_{na} has very little effect on the MVF evolution. A similar variation is observed in the stored energy ES in the three cases, as shown in Fig. 11. These trends of variation in the MVF and in the ES can be attributed to either the change in ε

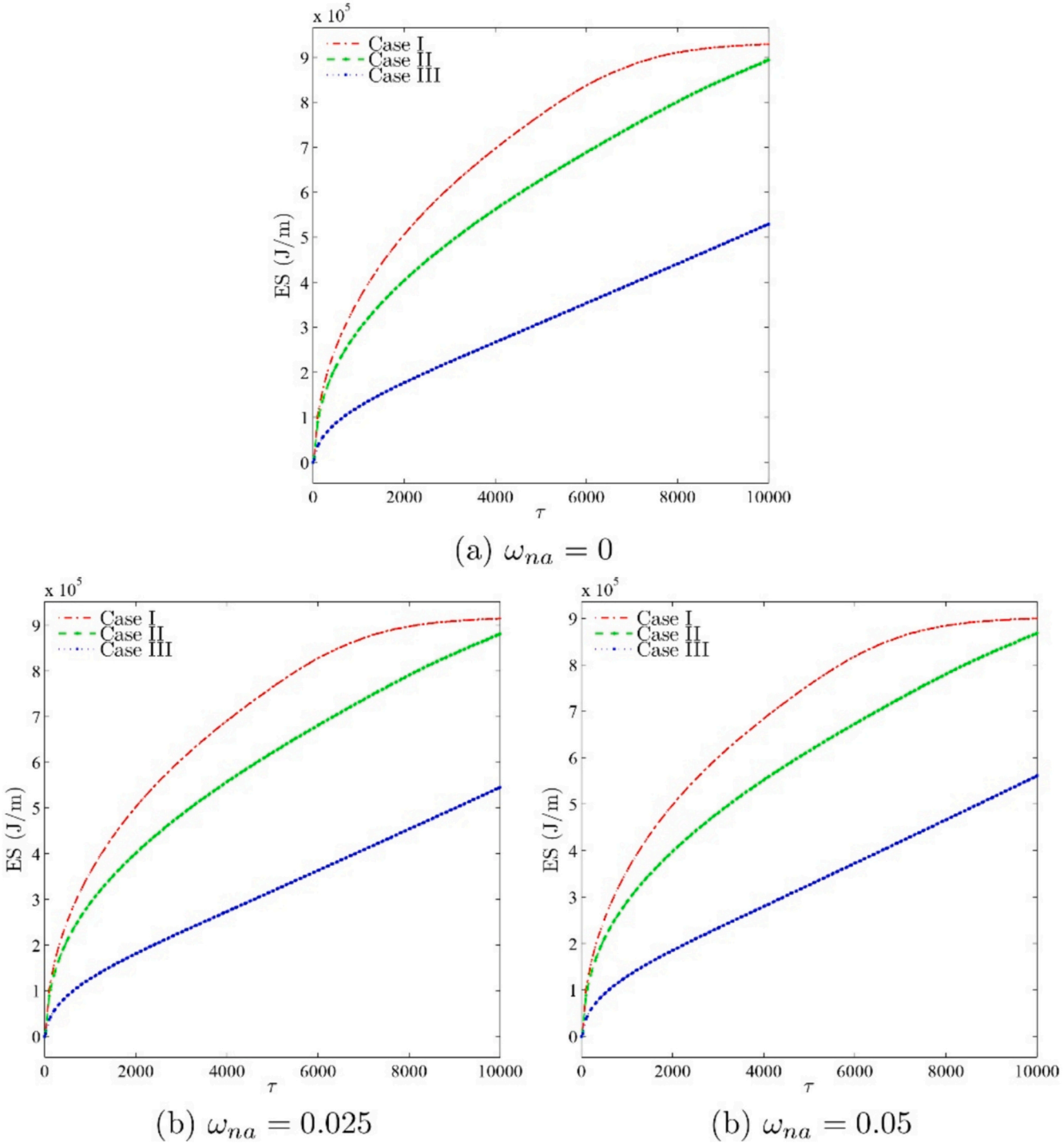

Fig. 11. Stored Energy (ES) evolution by different cases and different NeP fractions for $\varepsilon = 0.9$ and $N = 3$ (c).

or in N, so a detailed analysis of these two parameters' effect is undergone, therefore hereafter.

Fig. 12 illustrates the effect of the porosity ε on the streamlines and the isothermal contours. It is clear from the flow patterns that increasing ε has a significant negative effect on PCM melting. This is more evident in the bottom part of the enclosure, as PCM melting occurs in the upper part in all the configurations. Indeed, when the porosity is raised, the resistance to flow is improved, but the volume of the solid matrix is decreased. The part of heat conducted by this matrix to the solid PCM is then diminished. This is less intense in the upper part, where hot PCM is present due to convection. On the other hand, for low ε, the heat transfer in the bottom part is improved due to the increase in the volume of the solid matrix in the porous medium. This is evidenced by the isothermal contours, which show the best heat transfer in the lower region for $\varepsilon = 0.8$ compared to the other regions. Conversely, for $\varepsilon = 1$, in the absence of the porous medium, the flow is limited to the left and upper region of the cavity, while the PCM in the right lower part remains mainly in the solid state in the same period of time. The variation of MVF and ES as a function of time for different values of ε are depicted in Fig. 13.

Fig. 14 shows the flow and thermal patterns for various values of N. It can be seen that the patterns are similar in the center of the cavity for the three configurations. The difference occurs near the walls, but the

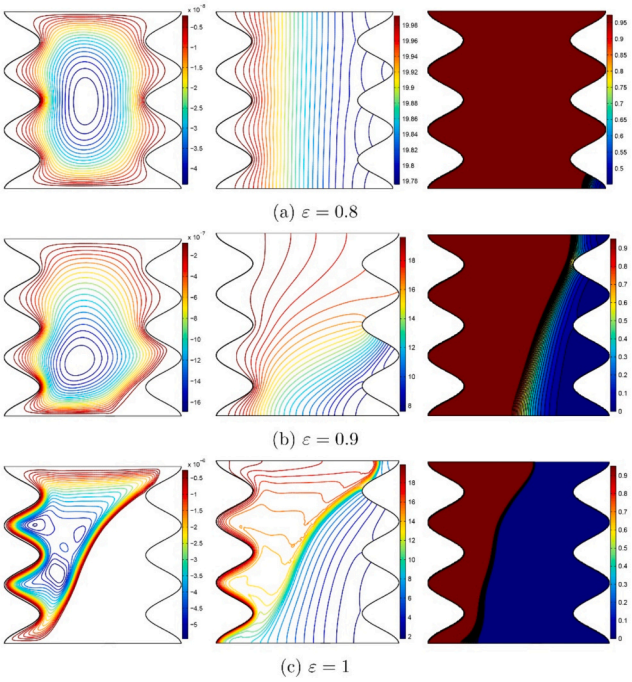

Fig. 12. Streamlines (left), isotherms (middle) and melting process (right) evolution by different ε for $\omega_{na} = 0.05$ and $N = 3$.

discrepancy is slight, as the PCM remains solid in the bottom right corner in all the cases. Increasing N raises the surface contact between the wall and the PCM, but this effect remains relatively marginal. Think there two antagonist effects when the undulation is increased, the thermal conductivity is enhanced as the surface contact is increased, but the intensity of the convective flow is decreased. The variation of MVF and ES with time, plotted in Fig. 15 for various values of N. As seen, after 10,000 of melting process, the melt fraction has reached about 90 %. Further melting takes a long time but does not provide much energy storage capacity. Fig. 15 shows that throughout melting, both MVF and ES are higher when N is raised and are maximum for $N = 3$ at which full melting is reached faster.

An optimization approach based on the Taguchi method is employed to evaluate the effect of the different parameters on PCM melting. The objective of this optimization is to maximize the melted volume fraction MVF. In particular, the melted volume fraction after 5000 s (MVF@5000 s) is selected as the optimization parameter. As the goal is to maximize the MVF, then the larger-the-better method is employed. The three tested parameters or control factors are ω_{na} (A), ε (B), and N (C). Each of these parameters is assigned three different values or levels,

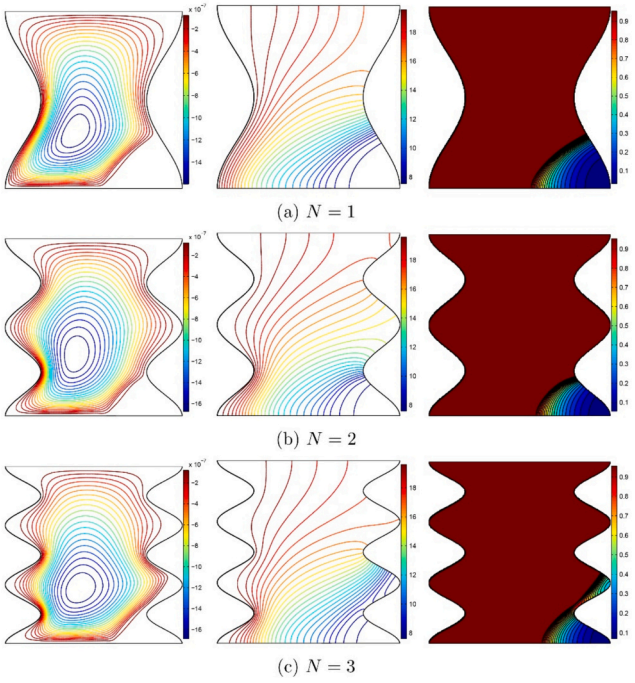

Fig. 14. Streamlines (left), isotherms (middle) and melting process (right) evolution by different N for $\omega_{na} = 0.05$ and $\varepsilon = 0.9$.

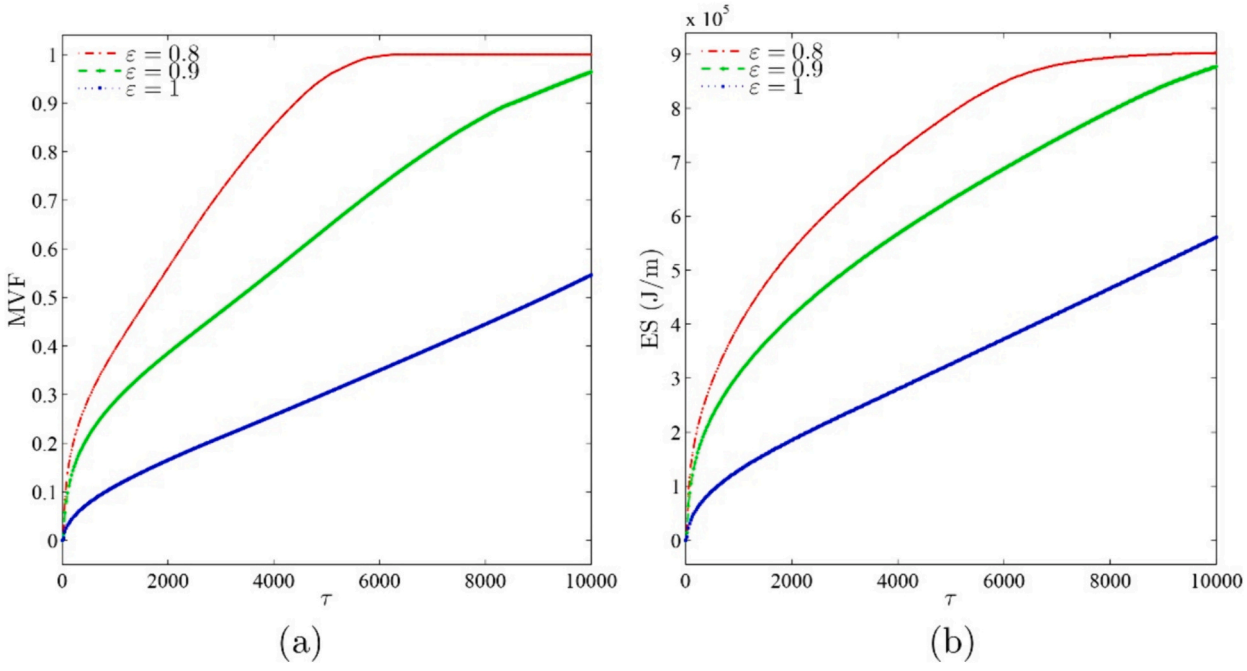

Fig. 13. Melt fraction (MVF) (a) and stored energy ES (b) evolution by time with different ε for $\omega_{na} = 0.05$ and $N = 3$.

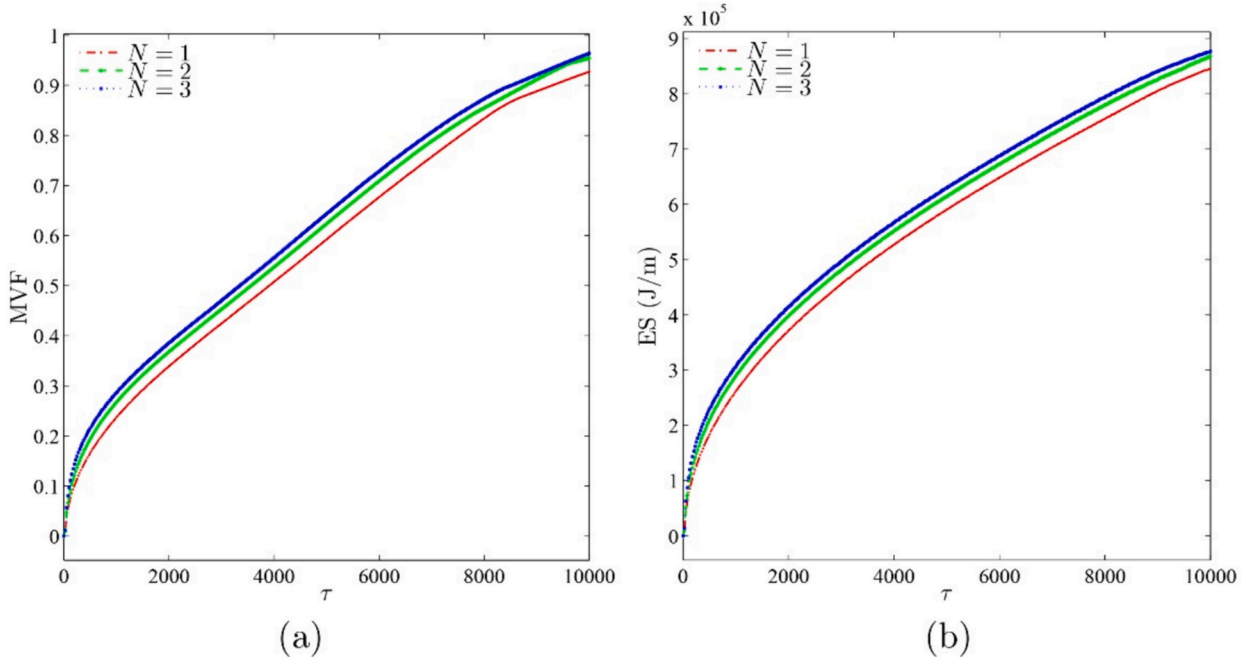

Fig. 15. Melt fraction MVF (a) and stored energy (ES) (b) evolution by time with different ε for $\omega_{na} = 0.05$ and $\varepsilon = 0.9$.

Table 3
The range and levels of control factors.

Factors	Description	Level 1	Level 2	Level 3
A	ω_{na} volume fraction	0.0	0.025	0.05
B	ε porosity	0.8	0.9	1.0
C	N wave number	1	2	3

as sown in Table 3. The L9 orthogonal array is used based on Taguchi's algorithm, and nine experiments are only performed to select the optimal values. The details of these experiments, as well as their outcomes, are presented in Table 7. Based on the optimization method, the optimal values of the control factors are given in Table 4: $\omega_{na} = 0.05$, $\varepsilon = 0.8$, and $N = 2$. In addition, a linear regression can be developed to approximate the MVF@5000 s as a function of the control factors:

$$\text{MVF@5000 s} = 3.3769 + 0.361\omega_{na} - 3.0866\varepsilon - 0.00041\,\text{N} \quad (18)$$

To further assess the degree of influence of each parameter on the result, an analysis based on the signal-to-noise ratio (SNR) is performed. The SNR is an indicator of the ratio of desired outcomes to the undesired ones. Table 6 lists the MVF@5000 s for the different levels of the control factor. It is clear that the greatest difference between the maximum and minimum values of the result is present in the variation of ε, while this difference is at the lowest in the variation of N. This discrepancy between the maximum and minimum is symbolized by the parameter δ. The same trend of variation is observed in the variation of the SNR for the different control factors and its corresponding value of δ, illustrated in Table 5 and Fig. 16. Here also, δ is maximal for ε and minimal for N. These observations suggest that the tested parameters can be classified by their decreasing influence in the following order: $\varepsilon > \omega_{na} > N$. The outcomes of Taguchi's analysis confirm thus the observations discussed in Figs. 7, 9, and 11.

5. Conclusion

The flow and thermal properties of a porous wavy channel filled with Coconut oil-CuO -aluminum metal foam were investigated. The impact of porosity, wave number and volumetric fraction of nanoparticles on

Table 5
The optimal combinations of variables.

Optimum Factors			Optimum MVF at 5000 s	
ω_{na}	ε	N	Taguchi prediction	Tested case
0.05	0.8	2	0.92	0.94152

Optimum A = 3, B = 1, and C = 2.

Table 4
Taguchi L9 table for an orthogonal combinations of variables.

Experiment number	Control Parameters			*MVF* at 5000 s	*ES* (*kJ/m*)	*P= ES/Time* (*kW/m*)	S/N Ratio
	ω_{na}	ε	N				
1	0.00	0.8	1	0.89992	772,380	154.476	−0.9159
2	0.00	0.9	2	0.61188	627,690	125.538	−4.2667
3	0.00	1	3	0.27754	310,050	62.01	−11.1335
4	0.025	0.8	2	0.90801	764,560	152.912	−0.8382
5	0.025	0.9	3	0.61767	621,260	124.252	−4.1849
6	0.025	1	1	0.29017	318,060	63.612	−10.7469
7	0.05	0.8	3	0.91628	756,730	151.346	−0.7594
8	0.05	0.9	1	0.62387	614,890	122.978	−4.0981
9	0.05	1	2	0.30334	326,140	65.228	−10.3614

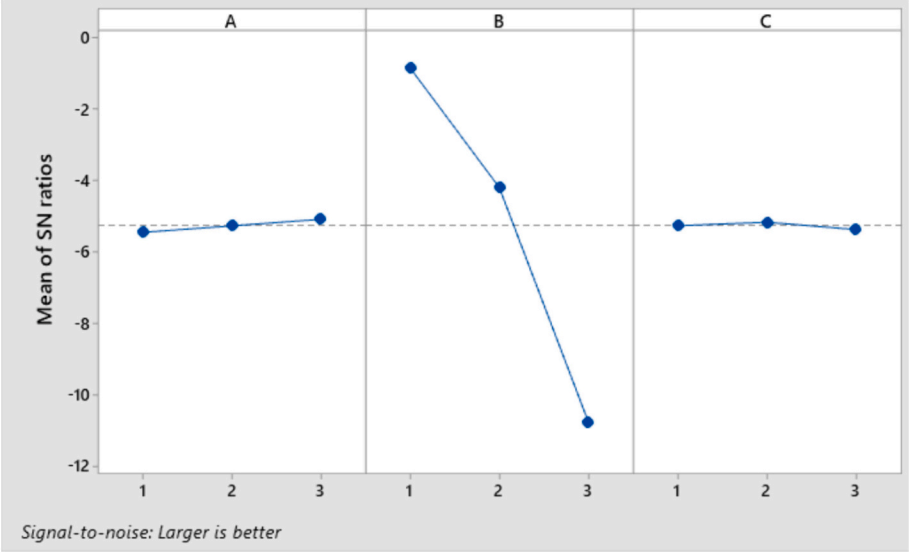

Fig. 16. The values of signal/noise (S/N) for different levels of variables. The optimum levels are: $A = 3$, $B = 1$, *and* $C = 2$.

Table 6
The means of MVF@5000 s.

Levels	ω_{na}	ε	N
Level 1	Level	A	B
Level 2	0.5964	0.9081	0.6047
Level 3	0.6053	0.6178	0.6077
δ	0.6145	0.2903	0.6038
Rank	0.0181	0.6177	0.0039

Table 7
The rank values of the parameters for MVF@5000 s.

Levels	ω_{na}	ε	N
Level 1	A	B	C
Level 2	−5.4387	−0.8378	−5.2537
Level 3	−5.2567	−4.1832	−5.1554
δ	−5.0730	−10.7473	−5.3593
Rank	0.3657	9.9094	0.2038

the melting rate, stored energy, and isotherms was explored. The Taguchi optimization technique was also utilized to maximize the MVF at 5000 s after thermal charging. The main outcomes of the present computational analysis are the following:

- The flow and thermal patterns initially show a conduction-dominated flow, which transitions into a phase where convective effects become more prominent. Flow separation is observed in the troughs of the wavy walls, with the right bottom corner being the last area to experience PCM melting due to weak heat transfer in that region.
- Increasing the porosity (ε) reduces the volume of the solid fraction within the porous medium and lessens the conduction of heat into the PCM, leading to decreased melting, particularly in the lower right half of the cavity.
- Altering the number of undulations on the wavy walls (N) affects the streamlines and isotherms close to the walls, yet it has a minimal impact on the overall flow and heat behaviors and the intensity of PCM melting.
- Based on Taguchi's optimization method, the following combination leads to the highest melted volume fraction after 5000 s: $\omega_{na} = 0.05$, $\varepsilon = 0.8$, and $N = 2$. Among these parameters, the porosity ε impacts the result most.

CRediT authorship contribution statement

Ammar I. Alsabery: Writing – review & editing, Writing – original draft, Validation, Project administration, Methodology, Investigation, Formal analysis, Data curation, Conceptualization. **Mohammad Ghalambaz:** Writing – review & editing, Writing – original draft, Visualization, Validation, Data curation, Conceptualization. **Ahmad Hajjar:** Writing – review & editing, Writing – original draft, Visualization, Validation, Data curation. **Obai Younis:** Writing – review & editing, Writing – original draft, Validation, Investigation. **Ali Akremi:** Writing – review & editing, Visualization. **Mehdi A. Fteiti:** Writing – review & editing, Writing – original draft, Validation, Methodology, Data curation. **Ishak Hashim:** Writing – review & editing, Writing – original draft, Supervision, Resources, Funding acquisition.

Declaration of competing interest

The authors declare that they have no known competing financial interests or personal relationships that could have appeared to influence the work reported in this paper.

Data availability

No data was used for the research described in the article.

Acknowledgements

The authors extend their appreciation to the Deanship of Scientific Research at Northern Border University, Arar, KSA for funding this research work through the project number NBU-FFR-2024-2246-02.

References

[1] A. Crespo, C. Barreneche, M. Ibarra, W. Platzer, Latent thermal energy storage for solar process heat applications at medium-high temperatures–a review, Sol. Energy 192 (2019) 3–34.
[2] M.M.A. Khan, N.I. Ibrahim, I. Mahbubul, H.M. Ali, R. Saidur, F.A. Al-Sulaiman, Evaluation of solar collector designs with integrated latent heat thermal energy storage: a review, Sol. Energy 166 (2018) 334–350.
[3] A. Agrawal, D. Rakshit, Review on thermal performance enhancement techniques of latent heat thermal energy storage (LHTES) system for solar and waste heat

recovery applications, in: New Research Directions in Solar Energy Technologies, Springer, 2021, pp. 411–438.
[4] A.A. Omara, Phase change materials for waste heat recovery in internal combustion engines: a review, Journal of Energy Storage 44 (2021) 103421.
[5] K. Reddy, V. Mudgal, T. Mallick, Review of latent heat thermal energy storage for improved material stability and effective load management, Journal of Energy Storage 15 (2018) 205–227.
[6] K. Faraj, M. Khaled, J. Faraj, F. Hachem, C. Castelain, Phase change material thermal energy storage systems for cooling applications in buildings: a review, Renew. Sust. Energ. Rev. 119 (2020) 109579.
[7] K. Du, J. Calautit, Z. Wang, Y. Wu, H. Liu, A review of the applications of phase change materials in cooling, heating and power generation in different temperature ranges, Appl. Energy 220 (2018) 242–273.
[8] J. Jaguemont, N. Omar, P. Van den Bossche, J. Mierlo, Phase-change materials (PCM) for automotive applications: a review, Appl. Therm. Eng. 132 (2018) 308–320.
[9] M.H. Abokersh, M. Osman, O. El-Baz, M. El-Morsi, O. Sharaf, Review of the phase change material (PCM) usage for solar domestic water heating systems (SDWHS), Int. J. Energy Res. 42 (2) (2018) 329–357.
[10] Z.A. Qureshi, H.M. Ali, S. Khushnood, Recent advances on thermal conductivity enhancement of phase change materials for energy storage system: a review, Int. J. Heat Mass Transf. 127 (2018) 838–856.
[11] A. Arshad, M. Jabbal, H. Faraji, P. Talebizadehsardari, M.A. Bashir, Y. Yan, Numerical study of nanocomposite phase change material-based heat sink for the passive cooling of electronic components, Heat Mass Transf. (2021) 1–15.
[12] A. Arshad, M. Jabbal, H. Faraji, P. Talebizadehsardari, M.A. Bashir, Y. Yan, Thermal performance of a phase change material-based heat sink in presence of nanoparticles and metal-foam to enhance cooling performance of electronics, Journal of Energy Storage 48 (2022) 103882.
[13] N.S. Bondareva, M.A. Sheremet, Effect of the time-dependent volumetric heat flux on heat transfer performance inside a heat sink based on the phase change materials, Clean Techn. Environ. Policy 23 (4) (2021) 1151–1160.
[14] N.S. Bondareva, B. Buonomo, O. Manca, M.A. Sheremet, Heat transfer performance of the finned nano-enhanced phase change material system under the inclination influence, Int. J. Heat Mass Transf. 135 (2019) 1063–1072.
[15] H.M. Al-Najjar, J.M. Mahdi, D.O. Bokov, N.B. Khedher, N.K. Alshammari, M. J. Catalan Opulencia, M.A. Fagiry, W. Yaïci, P. Talebizadehsardari, Improving the melting duration of a PV/PCM system integrated with different metal foam configurations for thermal energy management, Nanomaterials 12 (3) (2022) 423.
[16] F. Iachachene, Y. Halouane, L. Achab, Heat transfer enhancement in lid-driven cavity with rotating cylinder: exploring NEPCMs and magnetic field effects, International Communications in Heat and Mass Transfer 149 (2023) 107095.
[17] C. Revnic, T. Groşan, M. Sheremet, I. Pop, Numerical simulation of MHD natural convection flow in a wavy cavity filled by a hybrid cu-Al2O3-water nanofluid with discrete heating, Appl. Math. Mech. 41 (9) (2020) 1345–1358.
[18] K.B. Saleem, W. Al-Kouz, A. Chamkha, Numerical analysis of rarefied gaseous flows in a square partially heated two-sided wavy cavity with internal heat generation, J. Therm. Anal. Calorim. 146 (1) (2021) 311–323.
[19] N.V. Ganesh, Q.M. Al-Mdallal, G. Hirankumar, R. Kalaivanan, A.J. Chamkha, Buoyancy-driven convection of MWCNT–Casson nanofluid in a wavy enclosure with a circular barrier and parallel hot/cold fins, Alex. Eng. J. 61 (4) (2022) 3249–3264.
[20] N. Biswas, M.K. Mondal, D.K. Mandal, N.K. Manna, R.S.R. Gorla, A.J. Chamkha, A narrative loom of hybrid nanofluid-filled wavy walled tilted porous enclosure imposing a partially active magnetic field, Int. J. Mech. Sci. 107028 (2021).
[21] N. Biswas, D.K. Mandal, N.K. Manna, R.S.R. Gorla, A.J. Chamkha, Magnetohydrodynamic thermal characteristics of water-based hybrid nanofluid-filled non-Darcian porous wavy enclosure: effect of undulation, International Journal of Numerical Methods for Heat & Fluid Flow 32 (5) (2022) 1742–1777.
[22] A. Shenoy, M. Sheremet, I. Pop, Convective Flow and Heat Transfer from Wavy Surfaces: Viscous Fluids, Porous Media, and Nanofluids, CRC press, 2016.
[23] H. Cheradi, Z. Haddad, F. Iachachene, K. Mansouri, M. Arıcı, A comprehensive numerical study on melting performance in a storage cavity with partial metal foam integration: design and economic assessment, Journal of Energy Storage 85 (2024) 110985.
[24] Z. Haddad, F. Iachachene, M.A. Sheremet, E. Abu-Nada, Numerical investigation and optimization of melting performance for thermal energy storage system partially filled with metal foam layer: new design configurations, Appl. Therm. Eng. 223 (2023) 119809.
[25] A.M. Aly, Z. Raizah, A. Al-Hanaya, Double rotations between an inner wavy shape and a hexagonal-shaped cavity suspended by NEPCM using a time-fractional derivative of the ISPH method, International Communications in Heat and Mass Transfer 127 (2021) 105533.
[26] A.M. Aly, Z. Raizah, S. El-Sapa, H.F. Oztop, N. Abu-Hamdeh, Thermal diffusion upon magnetic field convection of nano-enhanced phase change materials in a permeable wavy cavity with crescent-shaped partitions, Case Studies in Thermal Engineering 101855 (2022).
[27] A.M. Aly, E.M. Mohamed, M.F. El-Amin, N. Alsedais, Double-diffusive convection between two different phases in a porous infinite-shaped enclosure suspended by nano encapsulated phase change materials, Case Studies in Thermal Engineering 26 (2021) 101016.
[28] S. Singh, B.S. Negi, Numerical thermal performance investigation of phase change material integrated wavy finned single pass solar air heater, Journal of Energy Storage 32 (2020) 102002.
[29] X. Ma, M. Sheikholeslami, M. Jafaryar, A. Shafee, T. Nguyen-Thoi, Z. Li, Solidification inside a clean energy storage unit utilizing phase change material with copper oxide nanoparticles, J. Clean. Prod. 245 (2020) 118888.
[30] F. Iachachene, Z. Haddad, E. Abu-Nada, M.A. Sheremet, Natural convection melting of phase change material in corrugated porous cavities, Sustain Energy Technol Assess 53 (2022) 102734.
[31] M.F. Osman, K. Sarath, M. Deepu, Studies on the melting dynamics of PCM in a semicircular cavity with straight and wavy heating surfaces, International Communications in Heat and Mass Transfer 151 (2024) 107249.
[32] S.K. Chaurasiya, S. Singh, High power and energy density of a wavy PCM unit embedded in a solar air heater utilizing fractional porous media, Appl. Therm. Eng. 236 (2024) 121843.
[33] A. Shahsavar, J. Khosravi, H.I. Mohammed, P. Talebizadehsardari, Performance evaluation of melting/solidification mechanism in a variable wave-length wavy channel double-tube latent heat storage system, Journal of Energy Storage 27 (2020) 101063.
[34] M. Boujelbene, S. Mehryan, A.M. Hussin, T. Yusaf, M. Shahabadi, M. Ghalambaz, Melting process investigation of a non-Newtonian phase change material containing multiwalled carbon nanotubes in a trapezoidal enclosure, International Communications in Heat and Mass Transfer 148 (2023) 107069.
[35] S.C. Kim, R. Prabakaran, D. Sakthivadivel, N. Thangapandian, A. Bhatia, P. Ganesh Kumar, Thermal transport properties of carbon-assisted phase change nanocomposite, fullerenes, Nanotubes and Carbon Nanostructures 28 (11) (2020) 925–933.
[36] M. Al-Jethelah, S. Ebadi, K. Venkateshwar, S. Tasnim, S. Mahmud, A. Dutta, Charging nanoparticle enhanced bio-based PCM in open cell metallic foams: an experimental investigation, Appl. Therm. Eng. 148 (2019) 1029–1042.
[37] M. Sheikholeslami, CuO-water nanofluid free convection in a porous cavity considering Darcy law, The European Physical Journal Plus 132 (1) (2017) 1–11.
[38] M.A. Sheremet, T. Grosan, I. Pop, Free convection in a square cavity filled with a porous medium saturated by nanofluid using Tiwari and Das' nanofluid model, Transp. Porous Media 106 (3) (2015) 595–610.
[39] D.A. Nield, A. Bejan, Convection in Porous Media, Springer Science & Business Media, 2006.
[40] J. Buongiorno, Convective transport in nanofluids, J. Heat Transf. 128 (3) (2006) 240–250.
[41] M. Sheikholeslami, M. Shamlooei, R. Moradi, Fe3O4-ethylene glycol nanofluid forced convection inside a porous enclosure in existence of coulomb force, J. Mol. Liq. 249 (2018) 429–437.
[42] D.A. Nield, A. Bejan, Convection in Porous Media, Springer, 2006.
[43] O. Meşalhy, K. Lafdi, A. Elgafy, K. Bowman, Numerical study for enhancing the thermal conductivity of phase change material (PCM) storage using high thermal conductivity porous matrix, Energy Convers. Manag. 46 (6) (2005) 847–867.
[44] H. Zheng, C. Wang, Q. Liu, Z. Tian, X. Fan, Thermal performance of copper foam/paraffin composite phase change material, Energy Convers. Manag. 157 (2018) 372–381.
[45] M. Gupta, V. Singh, R. Kumar, Z. Said, A review on thermophysical properties of nanofluids and heat transfer applications, Renew. Sust. Energ. Rev. 74 (2017) 638–670.
[46] H.C. Brinkman, The viscosity of concentrated suspensions and solutions, J. Chem. Phys. 20 (4) (1952) 571.
[47] H.Ş. Aybar, M. Sharifpur, M.R. Azizian, M. Mehrabi, J.P. Meyer, A review of thermal conductivity models for nanofluids, Heat Transfer Eng. 36 (13) (2015) 1085–1110.
[48] M. Bollhöfer, O. Schenk, R. Janalik, S. Hamm, K. Gullapalli, State-of-the-art sparse direct solvers, Parallel algorithms in computational science and engineering (2020) 3–33.
[49] M. Bollhöfer, A. Eftekhari, S. Scheidegger, O. Schenk, Large-scale sparse inverse covariance matrix estimation, SIAM J. Sci. Comput. 41 (1) (2019) A380–A401.
[50] B. Kamkari, H. Shokouhmand, F. Bruno, Experimental investigation of the effect of inclination angle on convection-driven melting of phase change material in a rectangular enclosure, Int. J. Heat Mass Transf. 72 (2014) 186–200.
[51] Z.-R. Li, N. Hu, J. Liu, R.-H. Zhang, L.-W. Fan, Revisiting melting heat transfer of nano-enhanced phase change materials (NePCM) in differentially-heated rectangular cavities using thermochromic liquid crystal (TLC) thermography, Int. J. Heat Mass Transf. 159 (2020) 120119.